DTU Library

A Massive Quiescent Galaxy in a Group Environment at z = 4.53

Kakimoto, Takumi; Tanaka, Masayuki; Onodera, Masato; Shimakawa, Rhythm; Wu, Po Feng; Gould, Katriona M.L.; Ito, Kei; Jin, Shuowen; Kubo, Mariko; Suzuki, Tomoko L.

Total number of authors:
13

[Link back to DTU Orbit](#)

A Massive Quiescent Galaxy in a Group Environment at $z = 4.53$

Takumi Kakimoto[1,2] , Masayuki Tanaka[1,2] , Masato Onodera[1,3] , Rhythm Shimakawa[4,5] , Po-Feng Wu[6,7,8] ,
Katriona M. L. Gould[9,10] , Kei Ito[11,16] , Shuowen Jin[9,12] , Mariko Kubo[13] , Tomoko L. Suzuki[14] , Sune Toft[9,10] ,
Francesco Valentino[9,15] , and Kiyoto Yabe[3]

[1] Department of Astronomical Science, The Graduate University for Advanced Studies, SOKENDAI, 2-21-1 Osawa, Mitaka, Tokyo 181-8588, Japan
takumi.kakimoto@grad.nao.ac.jp
[2] National Astronomical Observatory of Japan, 2-21-1 Osawa, Mitaka, Tokyo 181-8588, Japan
[3] Subaru Telescope, National Astronomical Observatory of Japan, National Institutes of Natural Sciences (NINS), 650 North A'ohoku Place, Hilo, HI 96720, USA
[4] Waseda Institute for Advanced Study (WIAS), Waseda University, 1-21-1, Nishi-Waseda, Shinjuku, Tokyo 169-0051, Japan
[5] Center for Data Science, Waseda University, 1-6-1, Nishi-Waseda, Shinjuku, Tokyo 169-0051, Japan
[6] Institute of Astrophysics, National Taiwan University, Taipei 10617, Taiwan
[7] Department of Physics and Center for Theoretical Physics, National Taiwan University, Taipei 10617, Taiwan
[8] Physics Division, National Center for Theoretical Sciences, Taipei 10617, Taiwan
[9] Cosmic Dawn Center (DAWN), Denmark
[10] Niels Bohr Institute, University of Copenhagen, Jagtvej 128, DK-2200 Copenhagen N, Denmark
[11] Department of Astronomy, School of Science, The University of Tokyo, 7-3-1, Hongo, Bunkyo-ku, Tokyo, 113-0033, Japan
[12] DTU Space, Technical University of Denmark, Elektrovej 327, DK-2800 Kgs. Lyngby, Denmark
[13] Astronomical Institute, Tohoku University, Aoba-ku, Sendai 980-8578, Japan
[14] Kavli Institute for the Physics and Mathematics of the Universe (WPI), The University of Tokyo Institutes for Advanced Study, The University of Tokyo, Kashiwa,
Chiba 277-8583, Japan
[15] European Southern Observatory, Karl-Schwarzschild-Str. 2, 85748 Garching, Germany

Abstract

We report on the spectroscopic confirmation of a massive quiescent galaxy at $z_{spec} = 4.53$ in the COSMOS field. The object was first identified as a galaxy with suppressed star formation at $z_{phot} \sim 4.65$ from the COSMOS2020 catalog. The follow-up spectroscopy with Keck/MOSFIRE in the K band reveals faint [O II] emission and the Balmer break, indicative of evolved stellar populations. We fit the spectral energy distribution using photometry and a spectrum to infer physical properties. The obtained stellar mass is high ($M_* \sim 10^{10.8} M_\odot$) and the current star formation rate is more than 1 dex below that of main-sequence galaxies at $z = 4.5$. Its star formation history suggests that this galaxy experienced rapid quenching from $z \sim 5$. The galaxy is among the youngest quiescent galaxies confirmed so far at $z_{spec} > 3$ with $z_{form} \sim 5.2$ (200 Myr ago), which is the epoch when 50% of the total stellar mass was formed. A unique aspect of the galaxy is that it is in an extremely dense region; there are four massive star-forming galaxies at $4.4 < z_{phot} < 4.7$ located within 150 physical kpc from the galaxy. Interestingly, three of them have virial radii that strongly overlap with that of the central quiescent galaxy (~ 70 kpc), suggesting that the overdensity region is likely the highest-redshift candidate of a dense group with a spectroscopically confirmed quiescent galaxy at the center. The group provides us with a unique opportunity to gain insights into the role of the group environment in quenching at $z \sim 5$, which corresponds to the formation epoch of massive elliptical galaxies in the local Universe.

Unified Astronomy Thesaurus concepts: Galaxy evolution (594); High-redshift galaxies (734); Galaxy quenching (2040); Quenched galaxies (2016); Galaxy groups (597); Galaxy environments (2029)

1. Introduction

Massive elliptical galaxies in the local Universe are known to be dominated by old stellar populations with little cold gas and dust and to exhibit no active ongoing star formation (e.g., Young & Scoville 1991; Gallazzi et al. 2005; Bellstedt et al. 2020). Since these massive galaxies likely have played a major role in cosmic star formation activities in the early Universe, it is very important to study their formation mechanisms. The star formation histories (SFHs) of massive elliptical galaxies inferred from spectroscopic observations show that they experienced an intense burst of star formation in the early

Universe and then rapidly quenched (stopped their star formation, Nelan et al. 2005; Thomas et al. 2005, 2010; Renzini 2006). However, the physical drivers of their starburst and subsequent quenching remain unclear, which makes this one of the most outstanding issues in the field of galaxy formation and evolution (Man & Belli 2018).

To elucidate these problems, a lot of effort has been put into searching for progenitors of local elliptical galaxies at high redshifts and examining them closer to the time of quenching. Over the last two decades, massive quiescent galaxies with no significant ongoing star formation at $z \sim 2$, which are likely the progenitors of local ellipticals, have been extensively studied (e.g., Cimatti et al. 2004; Glazebrook et al. 2004; Daddi et al. 2005; Cimatti et al. 2008; Kriek et al. 2009, 2019; Onodera et al. 2012, 2015; Toft et al. 2012; Whitaker et al. 2012; Belli et al. 2017, 2019; Morishita et al. 2019; Stockmann et al. 2020). These researches infer SFHs of the galaxies and confirm the evidence of starburst at $z > 3$ and a short quenching

---

[16] JSPS Research Fellow (PD).

timescale. These galaxies also have very large stellar masses ($M_* > 10^{11}\,M_\odot$) and compact sizes ($R_e < 2$ kpc) compared to their counterparts in the local Universe (e.g., van Dokkum et al. 2008; Cassata et al. 2011; Newman et al. 2012; van der Wel et al. 2014; Lustig et al. 2021).

Thanks to the recent development of sensitive near-infrared spectrographs, massive quiescent galaxies at up to $z \sim 4$ are spectroscopically confirmed (e.g., Glazebrook et al. 2017; Schreiber et al. 2018; Forrest et al. 2020a, 2020b; D'Eugenio et al. 2020, 2021; Valentino et al. 2020; Nanayakkara et al. 2024; Antwi-Danso et al. 2023; Tanaka et al. 2023). This epoch is consistent with the formation epoch inferred from the local elliptical galaxies (Thomas et al. 2010), and the identification of massive quiescent galaxies at $z > 4$ is critical to understanding their quenching mechanism. The number of sources confirmed at $z > 4$ is still relatively limited (Tanaka et al. 2019; Carnall et al. 2023b), but deep ground-based observations and new JWST spectroscopy are about to change the landscape. Also, recent cosmological simulations have difficulties in reproducing these galaxies (e.g., Schreiber et al. 2018; Cecchi et al. 2019; Guarnieri et al. 2019; Merlin et al. 2019; Valentino et al. 2020; Gould et al. 2023). Observational confirmations of massive quiescent galaxies at $z > 4$ are an important step in constraining models of galaxy formation.

In terms of the environment in which galaxies reside, it is known that elliptical galaxies dominate clusters of galaxies in the nearby Universe (e.g., Dressler 1980). This morphology–density relation shows that the surrounding environment may affect the physical properties of galaxies. Actually, massive quiescent galaxies dominate high-density environments at $z < 1$ (e.g., Gómez et al. 2003; Peng et al. 2010; Kawinwanichakij et al. 2017). These environments are basic components of large-scale structures in the nearby Universe, and examining the formation process by observing the high-redshift Universe is crucial. At $z > 2$, previous studies confirm "protoclusters," which are overdense regions of galaxies and are considered progenitors of local clusters (e.g., Capak et al. 2011; Toshikawa et al. 2014; Lemaux et al. 2018; Oteo et al. 2018; Harikane et al. 2019; Hu et al. 2021; Brinch et al. 2024). However, these protoclusters are often identified using star-forming galaxies as a tracer, and there are only a few systems with (confirmed) quiescent galaxies (e.g., Kalita et al. 2021; Kubo et al. 2021, 2022; McConachie et al. 2022; Ito et al. 2023). To understand the role of the environment in galaxy quenching at high redshift, it is crucial to examine more (proto) clusters and look for a sign of environmental effects in the act.

In this paper, we report the confirmation of a massive quiescent galaxy at $z = 4.53$ in the COSMOS field using the Keck/MOSFIRE spectrograph. The galaxy is located in a group environment, and we discuss a possible role of the environment in quenching at this high redshift for the first time. This paper is structured as follows. First, we introduce the target selection and spectroscopic follow-up observation in Section 2. In Section 3, physical properties of the quiescent galaxy inferred from spectral energy distribution (SED) fitting are summarized. Then, we discuss the galaxy's surrounding environment as well as its possible formation scenarios in Section 4. Finally, we conclude the paper in Section 5. We assume a Chabrier (2003) initial mass function (IMF) and a flat ΛCDM cosmology with $H_0 = 70\,\mathrm{km\,s^{-1}\,Mpc^{-1}}$, $\Omega_m = 0.3$, and $\Omega_\Lambda = 0.7$. All magnitudes are in the AB system (Oke & Gunn 1983).

2. Observation

2.1. Target Selection

Following the successful confirmation of the $z = 4.01$ quiescent galaxy in the Subaru/XMM-Newton Deep Field (Tanaka et al. 2019), we searched for massive quiescent galaxy candidates at $z > 4$ in the COSMOS field (Scoville et al. 2007). The COSMOS field is $\sim 2\,\mathrm{deg}^2$ and has been extensively observed from the X-ray to radio wavelengths, which allows us to obtain highly accurate photometric redshifts (photo-z's). As summarized in Ito et al. (2022), we applied our photo-z code (Tanaka 2015) to the COSMOS2020 CLASSIC catalog (Weaver et al. 2022). The code adopts the Bruzual & Charlot (2003) models, assuming exponentially declining SFHs (where the star formation rate is SFR$(t) \propto e^{-t/\tau}$), solar metallicities, the Calzetti et al. (2000) dust attenuation curve, and the Chabrier (2003) IMF. From the comparisons between photo-z's and spectroscopic redshifts from the literature, our photo-z's are confirmed to be accurate for massive quiescent galaxies at $2 < z < 4$ in the COSMOS field ($\sigma[\Delta z/(1 + z_{\mathrm{spec}})] = 0.03$, median$(\Delta z) = 0.011$: Ito et al. (2022), and references therein).

Based on this photo-z catalog, we applied the following cuts to select quiescent galaxy candidates: (1) $z_{\mathrm{phot}} > 4$ with little probability of being at lower redshifts to ensure that the Balmer break is in the K band, (2) $M_{*,\mathrm{c}} \gtrsim 5 \times 10^{10}\,M_\odot$ so that the target is sufficiently bright for us to trace its continuum ($M_{*,\mathrm{c}}$ refers to a stellar mass in the photo-z catalog), and (3) SFR inferred from the SED fitting is more than 1 dex below the star-forming main sequence (Schreiber et al. 2015). The last criterion is effectively similar to the rest-frame UVJ selection (Williams et al. 2009).

After careful visual screening, we identify a massive quiescent galaxy candidate at $z_{\mathrm{phot}} \sim 4.65$ with these cuts. Its SED exhibits a strong Balmer break, which suggests that the galaxy experienced an intense burst of star formation in the recent past and that its SFR has been declining since then (post-starburst phase). This object (COSMOS-1047519) is the subject of the paper. We note that there are other quiescent galaxy candidates, but most of them are very faint in the K_s band (having too high a redshift where the Balmer break is outside the K_s band or suffering from dust extinction). The selected candidate is the brightest candidate after the selection.

2.2. Spectroscopic Follow-up

We performed spectroscopic follow-up in the K band using the MOSFIRE spectrograph (McLean et al. 2010, 2012) on the Keck I telescope. We expected to fully cover the entire Balmer break from the photo-z. The target is rather faint with a K_s-band magnitude of 23.2 mag, and a long integration was required to identify absorption features. However, the weather did not fully cooperate and we could observe for roughly half of the allocated time (~ 9 hr on-source exposure). The observations were performed on three half-nights in 2022 March and April. We took ~ 100 pairs of the ABBA nodding with a 3 minutes exposure at each position. We nod $\pm 2''$ along the slit for good sky subtraction. We included two bright stars in the mask to monitor the sky conditions (see below). The mean seeing was around $0\rlap{.}''7$.

We reduced the data in the standard manner using the MOSFIRE Data Reduction Pipeline (DRP)[17] as well as

---

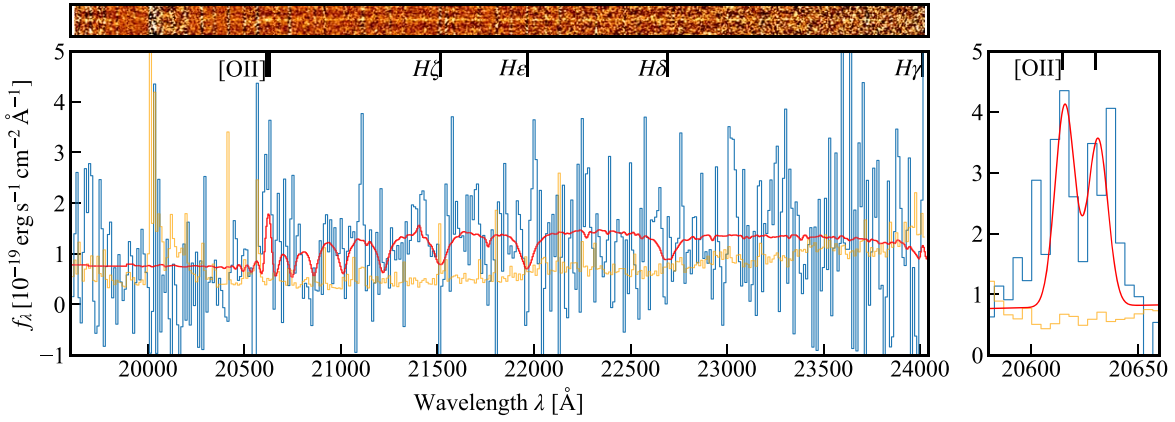[17] https://keck-datareductionpipelines.github.io/MosfireDRP/

Figure 1. Left: Keck/MOSFIRE K-band spectrum of COSMOS-1047519 smoothed over five pixels (10.8 Å). The top panel shows the two-dimensional spectrum, and the bottom panel shows the one-dimensional spectrum (the blue line) and the associated noise spectrum (the yellow line). The red line shows the best-fit model spectrum from `prospector` using spectrum and photometry (see Section 3). Right: blow-up of [O II] doublet lines smoothed over two pixels (4.3 Å). The red line represents the best-fit Gaussians.

custom-designed code. We reduced each A/B pair using DRP (flat-fielding, wavelength calibration, and background subtraction). The flux and the FWHM of the bright stars in each exposure were used to evaluate the observing conditions. We used the weight of flux/FWHM in the coaddition of the spectra to give more weight to exposures taken under better conditions. Four exposures were taken through thick clouds and were thus excluded from the coadd.

We observed the A0V star HD50046 as a spectrophotometric standard star on the first night of the observation. We applied the flux calibration and correction for the telluric absorption by comparing the spectrum of α Lyr from Hubble Space Telescope/CALSPEC (Bohlin et al. 2014) and the spectrum of the observed standard star. The CALSPEC spectrum was scaled to the standard star using the K_s-band photometry from the Two Micron All Sky Survey (Skrutskie et al. 2006).

We performed the optimal extraction (Horne 1986) to extract the 1D spectra from the 2D spectra. The spatial profile of the spectrum of the bright star was fit by a Gaussian, and it was used to extract the flux of the target galaxy. The error spectrum was estimated using the standard deviation of the background pixels in the same slit. Finally, the flux of the 1D spectrum is scaled to match the observed photometry to correct for the slit loss.

2.3. Redshift Confirmation

Figure 1 shows the observed 2D and 1D spectra rebinned over five pixels (10.8 Å). Due to the low signal-to-noise ratio (S/N) of the spectrum, we could not securely identify absorption lines. For example, the median S/N at 21000 Å $<$ $\lambda <$ 22000 Å is only 1.4 per 2.2 Å (original resolution). However, the spectrum exhibits a faint [O II] $\lambda\lambda$3727, 3729 emission with S/N$_{peak} \sim 5$. A blow-up of [O II] is shown in the right panel of Figure 1. This [O II] emission line provides a secure spectroscopic redshift for this object. We perform a Monte Carlo run to fit the [O II] doublet with two Gaussians and adopt the median as a point estimate and the 68% interval as an uncertainty, $z_{spec} = 4.5313 \pm 0.0005$. This redshift is consistent with the photo-z ($z_{phot} = 4.654^{+0.134}_{-0.104}$). Based on this redshift estimate, we discuss detailed properties of the galaxy in the next section.
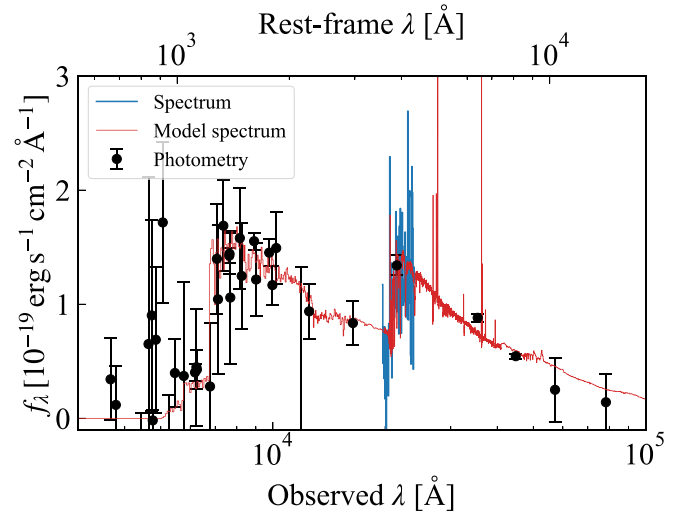

Figure 2. Spectral energy distribution of the target. The black points and error bars show the photometry from the COSMOS2020 catalog (Weaver et al. 2022), and the blue spectrum at $\sim 2\,\mu m$ is the MOSFIRE spectrum. The red spectrum is the best-fit model spectrum from `prospector`.

3. Inferred Physical Properties

3.1. SED Fitting

Figure 2 shows the SED of the galaxy. The black points are the photometry from the COSMOS2020 CLASSIC catalog with 40 bands from the u band to IRAC ch4 (Weaver et al. 2022). The blue spectrum is the MOSIFRE spectrum, which shows the prominent Balmer break, suggesting the post-starburst nature of this galaxy. The spectrum fully covers the break feature as expected, and we can accurately infer its SFH as shown below.

We fit the observed SED with `prospector` (Johnson et al. 2021). The MOSIFRE spectrum is rebinned over three pixels to gain S/N (e.g., the median S/N ~ 2.5 per 6.5 Å at 21000 Å $<$ $\lambda <$ 22000 Å). The `prospector` code uses the Flexible Stellar Population Synthesis model (Conroy et al. 2009; Conroy & Gunn 2010) to infer physical properties of the galaxy. We assume the Chabrier (2003) IMF, solar metallicities, the Madau (1995) model for absorption in the intergalactic medium, and the Calzetti et al. (2000) attenuation curve. The redshift is fixed to the spectroscopic redshift in the

Table 1
Inferred Physical Properties of the Quiescent Galaxy (COSMOS-1047519)

z_{phot}	z_{spec}	Model	$\log(M_*/M_\odot)$	$\mathrm{SFR_{SED}}$ $(M_\odot\,\mathrm{yr}^{-1})$	A_V (mag)	z_{form}	τ (Myr)	$\mathrm{SFR_{(O\,II)}}$ $(M_\odot\,\mathrm{yr}^{-1})$
(1)	(2)	(3)	(4)	(5)	(6)	(7)	(8)	(9)
		Delayed-tau	10.71 ± 0.04	$15.1^{+6.5}_{-5.2}$	$0.74^{+0.08}_{-0.09}$	$5.01^{+0.11}_{-0.08}$	$28.4^{+8.4}_{-6.0}$	$19.3^{+4.2}_{-3.2}$
$4.654^{+0.134}_{-0.104}$	4.5313 ± 0.0005	Log mass	10.77 ± 0.05	$11.2^{+8.5}_{-7.8}$	0.69 ± 0.12	$5.21^{+0.54}_{-0.28}$	...	$18.0^{+4.5}_{-3.5}$
		Dirichlet	10.79 ± 0.01	$8.76^{+6.85}_{-4.81}$	$0.61^{+0.13}_{-0.15}$	$5.36^{+0.38}_{-0.18}$	...	$16.0^{+4.5}_{-3.5}$

Notes. (1) Photometric redshift inferred from MIZUKI (Tanaka 2015). (2) Spectroscopic redshift from the Keck/MOSFIRE spectrum. (3) Name of the SFH model used in SED fitting (Johnson et al. 2021). (4) Inferred stellar mass. (5) SFR from the SED fitting averaged over $10^{7.5}$ yr. (6) V-band magnitude of dust attenuation from SED fitting. (7) Formation redshift at which the galaxy formed 50% of total stellar mass. Here, the lookback times from the SFH are converted into redshifts assuming the adopted cosmology (see Section 1). (8) Quenching timescale only in the delayed-tau model. (9) SFR from the flux of the [O II] emission corrected for dust attenuation.

fitting. As we detected the weak [O II] line, we include nebular emission in the model (fixed ionization parameter: $U = 0.01$).

We assume two models of SFH. One is a parametric SFH model with a linear rise of SFR followed by an exponential decrease ("delayed-tau model," $\mathrm{SFR}(t) \propto te^{-t/\tau}$). The parameter τ represents decay timescale of star formation. We choose this model because it is widely used and we can compare with other quiescent galaxies from the literature. The other model is a nonparametric SFH model, which allows the SFR in each age bin to vary, thus giving more flexibility in the SFH modeling. There are several priors to use in this nonparametric model, and we use the "log-mass prior" and "Dirichlet prior" (Leja et al. 2017, 2019). The log-mass prior is the most flexible model, but it could lead to a nonphysical SFH, such as causing an intense burst of star formation just after the Big Bang. Thus, we also use the Dirichlet prior, which forces the SFH to be smoother. As discussed below, the estimated SFHs are similar regardless of the SFH model used.

For all models, we apply the Markov Chain Monte Carlo method using emcee (Foreman-Mackey et al. 2013) to infer the best-fitting parameters and their associated errors. We use the log-uniform prior to the input parameters such as τ, age, and stellar mass. To be specific, in the parametric SFH model, the parameters are allowed to vary in the ranges $0.001\,\mathrm{Gyr} < \tau < 10\,\mathrm{Gyr}$, $0.13\,\mathrm{Gyr} < \mathrm{age} < 1.30\,\mathrm{Gyr}$, which is the age of the Universe at $z = 4.53$, and $10^9\,M_\odot < M_* < 10^{12}\,M_\odot$. For dust optical depth, we use the top-hat prior in the range $0 < A_V < 6$. In the nonparametric SFH model, we use the uniform prior to constrain the stellar masses of each age bin.

The best-fit model spectrum is shown in red in Figures 1 and 2. The model clearly shows the strong Balmer break in the K band, which indicates that the galaxy recently experienced a starburst and is now in the post-starburst phase. There is a relatively strong rest-frame UV continuum, implying that there is residual star formation activity in the galaxy. This is thus likely a young post-starburst and is likely being quenched. We will further discuss this point using physical properties inferred from the SED fit in the following subsection.

3.2. Inferred Physical Properties and SFH

From the SED fit, we infer physical properties of the galaxy such as stellar mass, SFR, dust optical depth, and SFH. These parameters are summarized in Table 1. We estimate the SFR from the SED fits and also from [O II] fit using two Gaussians. We use the following equation to convert the [O II] emission
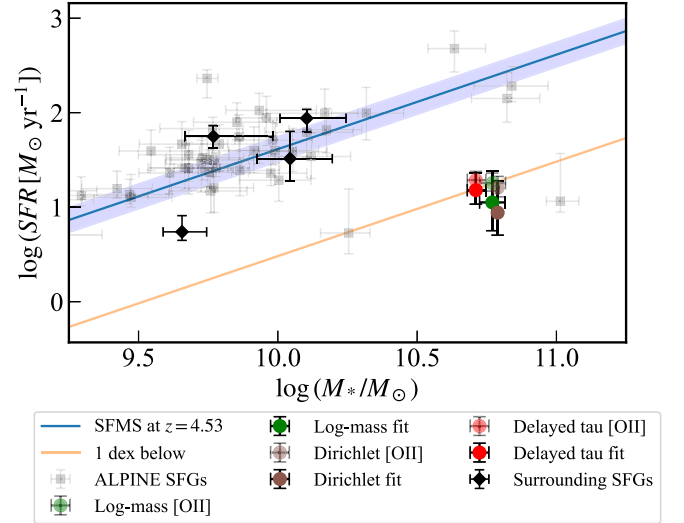

Figure 3. Stellar mass and SFR relation inferred from the three SFH models (color-coded symbols) compared to the star-forming main sequence (the blue line: Schreiber et al. 2015). The orange line shows the star-forming main sequence shifted by -1 dex. Inferred SFRs from both SED and [O II] emission corrected for dust are located around or below the orange line. The gray points are the normal star-forming galaxies at $z_{spec} \sim 4.5$ from the ALPINE survey (Béthermin et al. 2020; Faisst et al. 2020; Le Fèvre et al. 2020). There are two ALPINE galaxies below the orange line, but the one at $\log(M_*/M_\odot) \sim 10.3$ has a contaminating galaxy nearby, and the other one is possibly undergoing dust-obscured star formation (Faisst et al. 2020). We also include massive star-forming galaxies around the quiescent galaxy (the black diamonds, see discussion in Section 4).

flux to the SFR (Kewley et al. 2004; Schreiber et al. 2018):

$$\mathrm{SFR_{[O\,II]}}\,[M_\odot\,\mathrm{yr}^{-1}] = 1.59 \times 10^{-8} L_{[O\,II]}\,[L_\odot]. \quad (1)$$

We correct for dust attenuation of $L_{[O\,II]}$ using the dust optical depth from the best-fit model.

Figure 3 shows the location of the object on a diagram of SFR versus stellar mass. We also plot the normal star-forming galaxies from the ALPINE survey (Béthermin et al. 2020; Faisst et al. 2020; Le Fèvre et al. 2020) for reference. The galaxy is massive ($M_* \approx 6.0 \times 10^{10}\,M_\odot$), and has a very low SFR (SFR $\approx 10\,M_\odot\,\mathrm{yr}^{-1}$) averaged over $10^{7.5}$ yr. The estimated SFR is more than 1 dex below the star-forming main sequence (Schreiber et al. 2015). This supports our argument in the previous subsection that the galaxy is a massive quiescent galaxy based on Schreiber et al. (2018) criteria. If we perform the SED fitting without using the spectrum, the uncertainties of physical properties are about twice as large. In addition, the
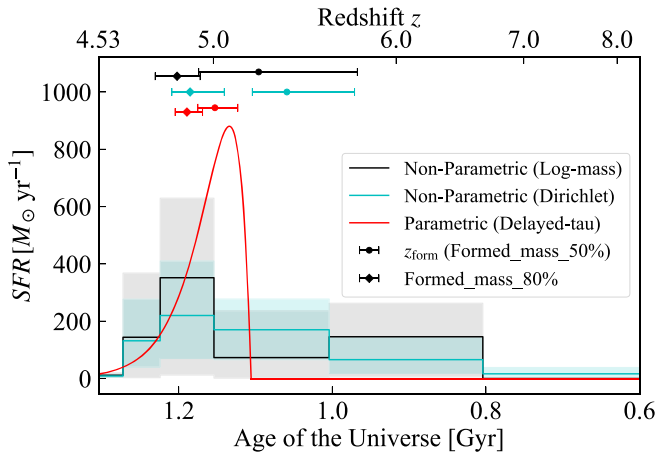
Figure 4. Inferred SFHs of the target: the black, blue, and red lines are the nonparametric SFH model with log-mass prior, nonparametric model with Dirichlet prior, and the delayed-tau model, respectively. The filled circles and diamonds with the error bars indicate the epochs when the galaxy formed 50% and 80% of the stars, respectively (the colors correspond to the SFH models).

Figure 5. Relation between formation redshift (z_{form}) at which the galaxy formed 50% of total stellar mass and observed redshift (z_{spec}). We plot COSMOS-1047519 (the red star) and spectroscopic samples of massive quiescent galaxies at $z > 3$ from previous research (Schreiber et al. 2018; Forrest et al. 2020b; Valentino et al. 2020; Nanayakkara et al. 2024; Carnall et al. 2023b). Carnall et al. (2023b) uses a mass-weighted mean formation time to define z_{form}.

height of the Balmer break cannot be fully determined by K_s-band photometry only, since the K_s bend is on the break. The spectrum, on the other hand, can firmly determine the break strength, resulting in a more precise age determination. Figure 3 also shows that the [O II]-based SFRs are higher than those obtained by SED fitting, which we interpret as a contribution from active galactic nuclei (AGNs) as we discuss in Section 3.4 (the model spectrum cannot reproduce [O II] either in Figure 1).

Figure 4 shows the inferred SFH of the galaxy. All of the SFH models are broadly consistent with each other, particularly during the quenching epoch; the galaxy experienced a rapid quenching process beginning around $z \sim 5$, which closely aligns with the SFH of massive elliptical galaxies (Thomas et al. 2010). The galaxy is young with a stellar age of 198^{+44}_{-32} Myr from the delayed-tau model, and the observed low SFR is consistent with the SFHs. Inferred physical parameters and SFH are not significantly changed by the age bins of the nonparametric SFH model. We conclude that this is a massive quiescent (or being quenched) galaxy and is likely a progenitor of massive elliptical galaxies in the local Universe.

The quiescence of the galaxy is also supported by multi-wavelength data. We look at the infrared to radio wavelengths to see a sign of dust-obscured star formation activity. However, the object is not detected in the far-infrared (S/N$_{IR} \sim 1.25$, SFR$_{IR} < 300 M_\odot$ yr^{-1} in the "Super-deblended" catalog: Jin et al. 2018) and radio ($f_{10\,cm} = 6.3 \times 10^{-4} \pm 2.8 \mu$Jy in Very Large Array 3 GHz: Smolčić et al. 2017). The object has not been observed by the Atacama Large Millimeter/submillimeter Array, and we do not have a strong constraint on dust emission at this point.

3.3. Comparison to Massive Quiescent Galaxies at z > 3

An interesting aspect of our quiescent galaxy is that it is currently experiencing ongoing suppression of star formation. The prominent Balmer break suggests an evolved stellar population, while the remaining UV continuum as well as the weak [O II] emission suggests that the galaxy is not completely quenched yet (Figures 1 and 2). The galaxy has a young luminosity-weighted age, and we must be observing the galaxy close to its primary formation epoch.
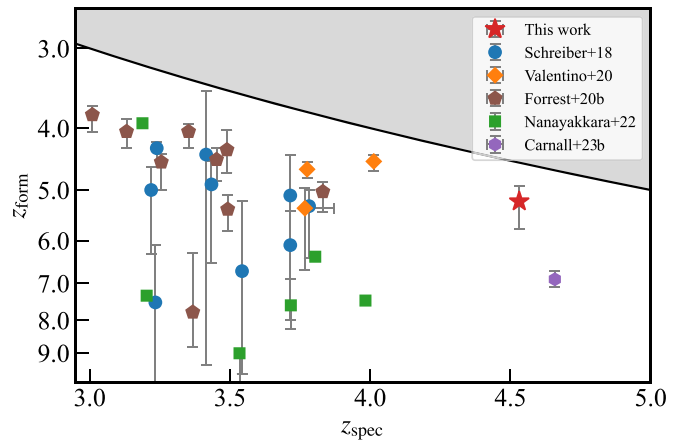
Figure 5 shows the relationship between the formation redshift (z_{form}) and observed redshift (z_{spec}) of massive quiescent galaxies at $z_{spec} > 3$ collected from the literature. The formation redshift is defined by the epoch at which the galaxy formed 50% of total stellar mass. This figure shows that massive quiescent galaxies at $z > 3$ have a wide range of formation epochs (also confirmed at $z < 3$: summarized in Kalita et al. 2021; Tacchella et al. 2022). Our galaxy is young and its formation redshift is close to the observed redshift. In addition, its formation redshift ($z_{form} \sim 5.2$) coincides with the inferred formation epoch of massive elliptical galaxies in the local Universe (Thomas et al. 2010). We thus speculate that the galaxy is a forming (or just formed) progenitor of nearby massive ellipticals, and a detailed study of the galaxy may provide us with a clue to the quenching physics. The other massive quiescent galaxies in the figure are generally older and more time has elapsed between the formation and observed epochs. For instance, Carnall et al. (2023b) confirm a massive quiescent galaxy at $z_{spec} = 4.658$. Compared to this galaxy, COSMOS-1047519 is younger and has a higher SFR and larger dust attenuation. However, the stellar mass and the peak SFR in its SFH are similar. Therefore, our galaxy is similar to the Carnall et al. (2023b) galaxy but we are closer to the quenching epoch.

The young age of our galaxy is likely due to a selection effect; we intentionally targeted the brightest candidate in the K_s band (which covers the Balmer break), and thus we tend to select galaxies with a prominent Balmer break, leading us to young post-starbursts. It is interesting that old quiescent galaxies show little dust attenuation ($A_V \sim 0$: e.g., Nanayakkara et al. 2024; Carnall et al. 2023b), while young ones suffer from a larger amount of attenuation ($A_V \sim 0.7$: this work, Valentino et al. 2020). This indicates that post-starburst galaxies have residual dust.

Based on the nonparametric SFH (Figure 4), the peak SFR of COSMOS-1047519 is SFR ~ 200–$400 M_\odot$ yr^{-1}. This is about 2–3 times higher than the SFR of star-forming main-sequence galaxies at $z = 5$ (Schreiber et al. 2015). If the galaxy experienced an intense starburst only once, starbursting galaxies are possible progenitors as suggested by previous
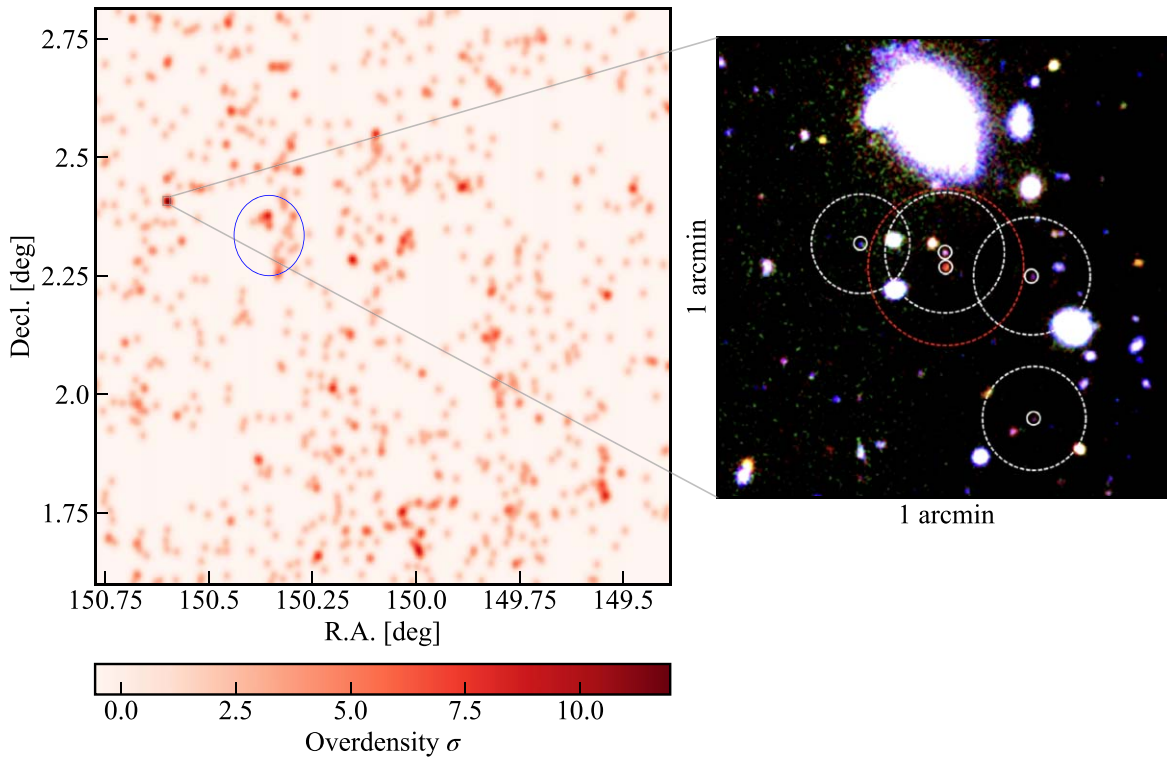
Figure 6. Distribution of massive ($M_{*,c} > 10^{10} M_\odot$ inferred from the photo-z catalog) galaxies at $4.4 < z_{\rm phot} < 4.7$ in the entire COSMOS field. The red color shows the density excess of the massive galaxy candidates smoothed over $30''$, which corresponds to the scale of the galaxy group candidate using kernel density estimation. The blue circle shows the massive protocluster at $z_{\rm spec} \sim 4.57$ ($R_{\rm proj} = 2$ Mpc: Lemaux et al. 2018). The right panel shows a pseudo-color image of the area around the quiescent galaxy (red: VISTA InfraRed CAMera/K_s band, green: VIRCAM/H band, blue: Hyper Suprime-Cam/i band, McCracken et al. 2012; Aihara et al. 2022). The five galaxies indicated with the white solid circles are the member candidates of this group centered on the quiescent galaxy. Our massive quiescent galaxy at $z = 4.53$ (the red point in the RGB image) exists in the densest region (12σ in the COSMOS field). The red and white dotted circles show the estimated virial radii of the quiescent galaxy and star-forming member candidates, respectively. The virial radii are estimated based on the stellar masses inferred from `prospector`.

research (e.g., Forrest et al. 2020a, 2020b; Valentino et al. 2020; Carnall et al. 2023b). Massive quiescent galaxies at $z \sim 2$ show similar properties to submillimeter galaxies (SMGs) at higher redshifts in terms of masses, effective radii, and number densities (Toft et al. 2014; Gómez-Guijarro et al. 2018). SMGs tend to have a larger SFR than the star-forming main sequence. By comparing the physical properties, the peak SFR in the SFH of our galaxy is consistent with that of SMGs that have similar stellar mass at $z \sim 5$ (e.g., da Cunha et al. 2015; Miettinen et al. 2017). Moreover, the quenching timescale for our quiescent galaxies is roughly 100 Myr, which is comparable to the gas depletion timescales of SMGs with similar specific SFRs (sSFRs) at $1 < z < 5$ (Gómez-Guijarro et al. 2022). This quenching timescale is defined as the period from when the galaxy reaches its peak SFR in the nonparametric SFH until the SFR decreases to 10% of that peak. Also, Zavala et al. (2022) summarize the redshift evolution of the gas depletion timescale of both starburst galaxies and normal star-forming galaxies and show that the timescale is shorter in the high-redshift Universe. Our galaxy's quenching timescale is consistent with the starburst galaxies' gas depletion timescale at $z \sim 5$. Thus, our work supports the scenario in which SMGs evolve into quiescent galaxies.

3.4. Comparisons with Simulations and the Role of AGNs

The Illustris TNG300 simulation (Pillepich et al. 2018; Nelson et al. 2019) is a large cosmological hydrodynamical simulation and reproduces the cosmic evolution from the early Universe to the local Universe. Thus, the simulation is a very useful tool to help us understand how massive galaxies form in the early Universe. We search for similar objects to COSMOS-1047519 in a snapshot at $z = 4.43$. However, there are no massive ($M_* > 10^{10.5} M_\odot$) quiescent galaxies with sSFR $< 10^{-9.5}$ yr^{-1}. Hartley et al. (2023) confirm the first quiescent galaxy in the TNG300 is at $z \sim 4.2$ although their definition of a quiescent galaxy is slightly different from ours (sSFR $< 10^{-10}$ yr^{-1}). They conclude that kinetic feedback from AGNs has a significant effect on the quenching process of quiescent galaxies reconstructed at $z \sim 4.2$. We note that COSMOS-1047519 is not detected in the deep X-ray observation ($L_{2-10\,{\rm keV}} < 5.1 \times 10^{43}$ erg s^{-1} in Chandra COSMOS Legacy: Civano et al. 2016), but this upper limit of X-ray luminosity does not rule out the possibility of low-luminosity AGNs in this galaxy.

Figure 1 shows that the model spectrum cannot fully reproduce the [O II] flux. Table 1 and Figure 3 also show that the [O II]-based SFR is higher than that from SED fitting. The observed excess suggests that AGNs may reside in the galaxy because [O II] is sensitive to ionization by (low-luminosity) AGNs as well as star formation (e.g., Yan et al. 2006). Maseda et al. (2021) find that more than half of massive quiescent galaxies at $z < 1$ exhibit [O II] lines and conclude that this feature is due to AGN activity. At $z > 2$, there are massive quiescent galaxies with AGNs (e.g., Kriek et al. 2009; Marsan et al. 2015; Schreiber et al. 2018; Kubo et al. 2022). Our galaxy may be a similar case, although it is located at a higher redshift. Future deep X-ray or JWST near-IR observations of AGN activity (confirming [O III], [N II], and Balmer lines) are necessary to identify or rule out low-luminosity AGNs.
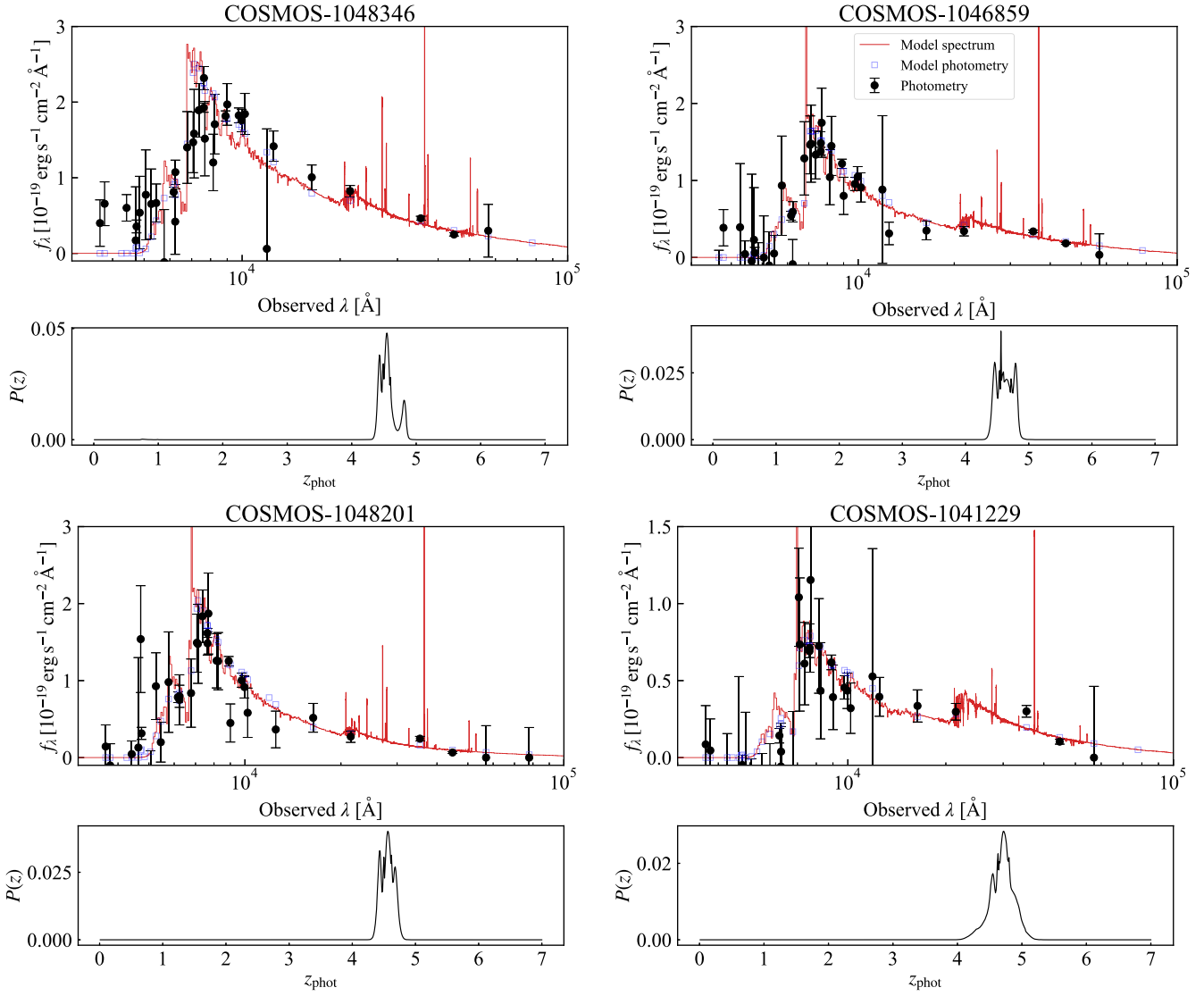
Figure 7. SEDs of the group member candidates. The black points show the photometry from the COSMOS2020 catalog (Weaver et al. 2022), and the red lines and blue squares indicate the model SEDs from MIZUKI (Tanaka 2015). The bottom panels show the probability distribution of photometric redshift. All galaxies have a large probability at $z_{\rm phot} \sim 4.5$.

Table 2
Coordinates (J2000) and VIRCAM/K_s-band Magnitudes of Massive Galaxy
Group Members

ID	R.A.	Decl.	m_{K_s} (mag)
1048346	$10^{\rm h}02^{\rm m}27\overset{\rm s}{.}099$	$+02°24'41\rlap{.}''607$	23.45
1046859	$10^{\rm h}02^{\rm m}26\overset{\rm s}{.}337$	$+02°24'38\rlap{.}''491$	24.85
1048201	$10^{\rm h}02^{\rm m}27\overset{\rm s}{.}838$	$+02°24'42\rlap{.}''755$	25.13
1041229	$10^{\rm h}02^{\rm m}26\overset{\rm s}{.}318$	$+02°24'19\rlap{.}''907$	24.72
1047519	$10^{\rm h}02^{\rm m}27\overset{\rm s}{.}091$	$+02°24'39\rlap{.}''672$	23.16

4. Group Environment around the Quiescent Galaxy

4.1. Overdensity in the Surrounding Structure

To gain deeper insights into quenching physics, we investigate the environment of our galaxy. We select massive ($M_{*,\rm c} > 10^{10} M_\odot$) galaxies regardless of SFRs at $4.4 < z_{\rm phot} < 4.7$ from the photo-z catalog in the COSMOS field (Section 2.1: Ito et al. 2022). The inset of Figure 6 shows a blow-up around

the quiescent galaxy (QG). There is a companion galaxy ($z_{\rm phot} = 4.535^{+0.168}_{-0.105}$) right next to it with a separation of $2''$. Furthermore, there are three massive star-forming galaxies (SFGs) ($z_{\rm phot} = 4.57$–4.69) within $23''$ or 151 kpc on a physical scale. We recall that the quiescent galaxy has a photo-z of 4.65. We summarize the SEDs and probability distributions of photo-z inferred from MIZUKI (Tanaka 2015) in Figure 7, and the coordinates in J2000 are summarized in Table 2. Each SED shows that all member candidates have bluer SEDs than the quiescent galaxy. The probability distributions show that all galaxies have the highest probability at $z_{\rm phot} \sim 4.5$, and most of them have consistent photometric redshifts within 1σ of the quiescent galaxy. These photo-z's are also consistent with the COSMOS2020 catalog.

To evaluate the physical properties of these SFGs and the QG homogeneously, we perform the SED fitting analysis of four SFGs by prospector using a parametric SFH model (delayed-tau model with the same priors as those used for the QG). The inferred physical properties are summarized in Table 3. The SFGs are normal star-forming galaxies (their locations on a diagram of SFR versus stellar mass are shown in Figure 3 as black diamonds) but their stellar masses are smaller

Table 3
Inferred Physical Properties of Massive Galaxy Group Members

ID	z_{phot}	z_{spec}	θ_{sep} (arcsec)	θ_{sep} (kpc)	$\log(M_*/M_\odot)$	SFR_{SED} ($M_\odot$ yr^{-1})	$\log(M_h/M_\odot)$	r_{200} (kpc)
(1)	(2)	(3)	(4)	(5)	(6)	(7)	(8)	(9)
1048346	$4.535^{+0.168}_{-0.105}$	⋯	1.94	12.8	10.10 ± 0.13	$87.1^{+19.0}_{-28.2}$	$11.91^{+0.76}_{-0.63}$	$51.8^{+40.5}_{-19.9}$
1046859	$4.630^{+0.118}_{-0.114}$	⋯	11.36	75.0	10.04 ± 0.14	$32.7^{+21.7}_{-17.8}$	$11.88^{+0.76}_{-0.64}$	$50.5^{+39.5}_{-19.6}$
1048201	$4.570^{+0.077}_{-0.075}$	⋯	11.61	76.4	9.66 ± 0.09	$5.48^{+2.18}_{-1.14}$	$11.66^{+0.70}_{-0.59}$	$42.7^{+30.1}_{-15.4}$
1041229	$4.693^{+0.103}_{-0.104}$	⋯	22.91	150.8	9.77 ± 0.18	$56.0^{+14.8}_{-16.1}$	$11.72^{+0.77}_{-0.62}$	$44.8^{+35.6}_{-16.8}$
1047519[a]	$4.654^{+0.134}_{-0.104}$	4.5313 ± 0.0005	⋯	⋯	10.71 ± 0.04	$15.1^{+6.5}_{-5.2}$	$12.26^{+0.74}_{-0.63}$	$67.5^{+51.3}_{-25.8}$

Notes. (1) Object ID of member galaxies from the COSMOS2020 CLASSIC catalog (Weaver et al. 2022). (2) Photometric redshift estimated from MIZUKI (Tanaka 2015). (3) Spectroscopic redshift of COSMOS-1047519. (4) Angular separation between COSMOS-1047519 and SFGs. (5) Projected physical distance between COSMOS-1047519 and SFGs. (6) Inferred stellar mass from prospector. (7) Inferred SFR from prospector. (8) The halo mass estimated from the stellar-to-halo mass relation (Shuntov et al. 2022). (9) Virial radius estimated from the halo mass of each galaxy.
[a] The physical properties of the QG are obtained from prospector using the delayed-tau model.

than our original estimates from our photo-z code. Yet, these values still satisfy the 70% completeness limit of SFGs at $z = 4.5$ ($M_* > 10^{9.37} M_\odot$, Weaver et al. 2023). The quiescent galaxy has the largest stellar mass, and this environment may be the highest-redshift galaxy group with a spectroscopically confirmed quiescent galaxy at the center.

To evaluate the significance of this overdensity of massive galaxies, we make a density plot in Figure 6. This plot is obtained by using the Gaussian kernel density estimation method. The galaxy distribution in the entire COSMOS field is smoothed over 30″ (200 physical kpc at $z = 4.5$, which roughly corresponds to the scale of this overdensity region). Our sample here is complete for SFGs but not for QGs (Weaver et al. 2023), and we may be missing low-mass QGs if there are any. SFGs significantly outnumber QGs at these redshifts and missing low-mass QGs will not strongly affect the density field. We find that our galaxy is located in a highly significant (12σ) overdensity region, and this structure turns out to be the densest region of massive galaxies at $4.4 < z_{phot} < 4.7$ in the COSMOS field. On the other hand, if the galaxy distribution is smoothed over 2′.5 (1 physical Mpc at $z = 4.5$), the region is a less significant (2.2σ) overdensity. This kernel density does not follow the Gaussian distribution, and the absolute significance is not very important. We also estimate the excess of galaxy density using the fifth-nearest-neighbor method, which yields a density distribution more similar to Gaussian and obtains 180σ. The group still remains the densest region in the entire COSMOS field. Thus, the group is very compact. For comparison, we indicate in Figure 6 a massive protocluster at $z \sim 4.57$ with the blue circle (Lemaux et al. 2018). As can be seen, the protocluster is much more extended than our group and on the scale of megaparsecs. The structure and size of our group are really different from those of typical protoclusters at this high redshift (Overzier 2016 for a review).

4.2. Halo Mass and Virial Radius

While we have not spectroscopically confirmed the redshifts of the SFGs yet, we make an attempt to infer the halo mass of each member and see whether they can be physically associated. We use the stellar-to-halo mass relation (SHMR) observed in the COSMOS field at $4.5 < z < 5.5$ (Shuntov et al. 2022) to estimate the halo mass from the stellar mass based on prospector, assuming that each member is a central galaxy. Estimated values are summarized in Table 3, column (8). The

most massive member (quiescent galaxy) has $M_h \sim 10^{12.3} M_\odot$, which is slightly smaller than the galaxy group at $z \gtrsim 3$ from previous research ($M_h \gtrsim 10^{13}$: e.g., Miller et al. 2018; Hill et al. 2020; Daddi et al. 2021). Next, we translate the halo mass into the virial radius. Here, we use the radius r_{200} (Carlberg et al. 1997) as the virial radius. Column (9) of Table 3 summarizes the virial radii of the member candidates. The dotted circles in the right panel of Figure 6 show that the virial radii of the member candidates significantly overlap. Two SFGs are just outside the virial radius of the quiescent galaxy in Figure 6, but they are actually consistent with being inside it within the uncertainties (see Table 3). The bottom right galaxy is outside it, but there is intrinsic scatter in the SHMR. These three or four galaxies likely form a group with the quiescent galaxy at the center. Spectroscopic confirmations of these member candidates are required for further characterization of the group environment.

4.3. Possible Formation Scenarios of the QG

As discussed earlier, COSMOS-1047519 is quenched very recently (or is being quenched currently). The group is thus an ideal object in which to examine the role of environments, especially for quenching. From the discussion in Sections 3.3 and 3.4, the quiescent galaxy experienced intense star formation ($\sim$200–400 $M_\odot$ yr^{-1}), and then rapid quenching started at $z \sim 5$. The peak SFR and quenching timescale from the SFH are similar to the SMG's SFR and gas depletion timescale at $z \sim 5$, respectively. Also, the K-band spectrum of the quiescent galaxy shows the excess of [O II] emission compared to the model spectrum from prospector, and this galaxy may harbor a low-luminosity AGN. Combining these points, the star formation and AGN activities induced by the galaxy–galaxy interactions and mergers drive the quenching of this quiescent galaxy. For example, observational and theoretical studies argue that minor mergers and galaxy interactions increase star formation efficiency and AGN activity (e.g., Hopkins et al. 2008; Brodwin et al. 2013; Coogan et al. 2018; Gómez-Guijarro et al. 2018). Also, previous studies confirm that gas mass fractions of QGs are significantly lower than those of SFGs (e.g., Sargent et al. 2015; Bezanson et al. 2019; Whitaker et al. 2021; Williams et al. 2021; Suzuki et al. 2022). Thus, it is possible that the quick gas depletion due to starburst is responsible for quenching.

Shimakawa et al. ([2018](#)) suggest that group/cluster environments have evolved stellar populations, and AGN feedback suppresses the star formation of member galaxies at high redshift ($2 < z < 3$). Chiang et al. ([2017](#)) argue that significant group- or cluster-sized cores (with the scale of r_{200}) would be the first region to show the galaxy quenching. Our group candidate has a scale comparable to these cores, and the quenching observed in this group environment at $z > 4$ is probably consistent with the core-scale quenching. Our work suggests this core-scale quenching has already occurred at $z > 4$ by gas consumption due to the starburst and/or AGN feedback. Furthermore, recent JWST observations confirm compact galaxy groups at $5 < z < 8$ (e.g., Hashimoto et al. [2023](#); Helton et al. [2024](#); Jin et al. [2023](#); Morishita et al. [2023](#); Sun et al. [2024](#)). Member galaxies are mostly low-mass SFGs, but Helton et al. ([2024](#)) show that more massive galaxies with larger SFR populate the overdensity region compared to the field. Therefore, the formation of galaxy groups with a QG at $z = 4.5$ could result from the evolution of such very high-redshift compact galaxy groups.

5. Conclusion

We present the spectroscopic confirmation of a massive quiescent galaxy at $z = 4.53$ based on the Keck/MOSFIRE observation. We confirm a very large stellar mass and a very low SFR from the extensive SED fitting using both the photometry and spectrum. The estimated SFR is more than 1 dex below the star-forming main sequence at $z = 4.5$. The SFH of the galaxy inferred from the SED fitting indicates rapid quenching with a timescale of ~ 100 Myr from $z \sim 5$.

To constrain physical drivers of the starburst and subsequent quenching, we compare the properties of this object with those of quiescent galaxies from the literature. The galaxy is one of the youngest quiescent galaxies from the formation redshift; this is an interesting object to aid in understanding the physical processes responsible for the suppression of star formation. The fact that the quenching timescale of the galaxy is comparable to the gas depletion timescale of SMGs at similar redshift indicates that the quenching is simply due to gas consumption. Also, the observational excess of [O II] indicates the existence of low-luminosity AGNs. In addition, the galaxy is found to be located in the group environment, which includes a companion galaxy at $2''$ (13 physical kpc). These findings suggest that gas depletion due to the starburst and/or AGN feedback triggered by galaxy–galaxy interactions or mergers may be responsible for quenching.

We can say that in Figure 5 we are clearly approaching the formation epoch of the massive quiescent galaxies. This is an exciting redshift regime to directly unveil the quenching physics. Recent JWST observations confirm quiescent galaxies at these redshifts (Carnall et al. [2023b](#)) as well as a large number of the quiescent galaxy candidates (Carnall et al. [2023a](#); Long et al. [2023](#); Valentino et al. [2023](#)). Upcoming imaging and spectroscopic observations will place a more stringent constraint on the physical mechanism of quenching and the detailed SFH in the near future.

ORCID iDs

Takumi Kakimoto ● https://orcid.org/0000-0003-2918-9890
Masayuki Tanaka ● https://orcid.org/0000-0002-5011-5178
Masato Onodera ● https://orcid.org/0000-0003-3228-7264
Rhythm Shimakawa ● https://orcid.org/0000-0003-4442-2750
Po-Feng Wu ● https://orcid.org/0000-0002-9665-0440
Katriona M. L. Gould ● https://orcid.org/0000-0003-4196-5960
Kei Ito ● https://orcid.org/0000-0002-9453-0381
Shuowen Jin ● https://orcid.org/0000-0002-8412-7951
Mariko Kubo ● https://orcid.org/0000-0002-7598-5292
Tomoko L. Suzuki ● https://orcid.org/0000-0002-3560-1346
Sune Toft ● https://orcid.org/0000-0003-3631-7176
Francesco Valentino ● https://orcid.org/0000-0001-6477-4011
Kiyoto Yabe ● https://orcid.org/0000-0001-6229-4858

References

Aihara, H., AlSayyad, Y., Ando, M., et al. 2022, PASJ, 74, 247
Antwi-Danso, J., Papovich, C., Esdaile, J., et al. 2023, arXiv:2307.09590
Astropy Collaboration, Price-Whelan, A. M., Sipőcz, B. M., et al. 2018, AJ, 156, 123
Astropy Collaboration, Robitaille, T. P., Tollerud, E. J., et al. 2013, A&A, 558, A33
Belli, S., Newman, A. B., & Ellis, R. S. 2017, ApJ, 834, 18
Belli, S., Newman, A. B., & Ellis, R. S. 2019, ApJ, 874, 17
Bellstedt, S., Robotham, A. S. G., Driver, S. P., et al. 2020, MNRAS, 498, 5581
Béthermin, M., Fudamoto, Y., Ginolfi, M., et al. 2020, A&A, 643, A2
Bezanson, R., Spilker, J., Williams, C. C., et al. 2019, ApJL, 873, L19
Bohlin, R. C., Gordon, K. D., & Tremblay, P. E. 2014, PASP, 126, 711
Brinch, M., Greve, T. R., Sanders, D. B., et al. 2024, MNRAS, 527, 6591
Brodwin, M., Stanford, S. A., Gonzalez, A. H., et al. 2013, ApJ, 779, 138
Bruzual, G., & Charlot, S. 2003, MNRAS, 344, 1000
Calzetti, D., Armus, L., Bohlin, R. C., et al. 2000, ApJ, 533, 682
Capak, P. L., Riechers, D., Scoville, N. Z., et al. 2011, Natur, 470, 233
Carlberg, R. G., Yee, H. K. C., & Ellingson, E. 1997, ApJ, 478, 462
Carnall, A. C., McLeod, D. J., McLure, R. J., et al. 2023a, MNRAS, 520, 3974
Carnall, A. C., McLure, R. J., Dunlop, J. S., et al. 2023b, Natur, 619, 716
Cassata, P., Giavalisco, M., Guo, Y., et al. 2011, ApJ, 743, 96
Cecchi, R., Bolzonella, M., Cimatti, A., & Girelli, G. 2019, ApJL, 880, L14

Chabrier, G. 2003, PASP, 115, 763
Chiang, Y. K., Overzier, R. A., Gebhardt, K., & Henriques, B. 2017, ApJL, 844, L23
Cimatti, A., Cassata, P., Pozzetti, L., et al. 2008, A&A, 482, 21
Cimatti, A., Daddi, E., Renzini, A., et al. 2004, Natur, 430, 184
Civano, F., Marchesi, S., Comastri, A., et al. 2016, ApJ, 819, 62
Conroy, C., & Gunn, J. E. 2010, ApJ, 712, 833
Conroy, C., Gunn, J. E., & White, M. 2009, ApJ, 699, 486
Coogan, R. T., Daddi, E., Sargent, M. T., et al. 2018, MNRAS, 479, 703
da Cunha, E., Walter, F., Smail, I. R., et al. 2015, ApJ, 806, 110
Daddi, E., Renzini, A., Pirzkal, N., et al. 2005, ApJ, 626, 680
Daddi, E., Valentino, F., Rich, R. M., et al. 2021, A&A, 649, A78
D'Eugenio, C., Daddi, E., Gobat, R., et al. 2020, ApJL, 892, L2
D'Eugenio, C., Daddi, E., Gobat, R., et al. 2021, A&A, 653, A32
Dressler, A. 1980, ApJ, 236, 351
Faisst, A. L., Schaerer, D., Lemaux, B. C., et al. 2020, ApJS, 247, 61
Foreman-Mackey, D., Hogg, D. W., Lang, D., & Goodman, J. 2013, PASP, 125, 306
Forrest, B., Annunziatella, M., Wilson, G., et al. 2020a, ApJL, 890, L1
Forrest, B., Marsan, Z. C., Annunziatella, M., et al. 2020b, ApJ, 903, 47
Gallazzi, A., Charlot, S., Brinchmann, J., White, S. D. M., & Tremonti, C. A. 2005, MNRAS, 362, 41
Glazebrook, K., Abraham, R. G., McCarthy, P. J., et al. 2004, Natur, 430, 181
Glazebrook, K., Schreiber, C., Labbé, I., et al. 2017, Natur, 544, 71
Gómez, P. L., Nichol, R. C., Miller, C. J., et al. 2003, ApJ, 584, 210
Gómez-Guijarro, C., Elbaz, D., Xiao, M., et al. 2022, A&A, 659, A196
Gómez-Guijarro, C., Toft, S., Karim, A., et al. 2018, ApJ, 856, 121
Gould, K. M. L., Brammer, G., Valentino, F., et al. 2023, AJ, 165, 248
Guarnieri, P., Maraston, C., Thomas, D., et al. 2019, MNRAS, 483, 3060
Harikane, Y., Ouchi, M., Ono, Y., et al. 2019, ApJ, 883, 142
Harris, C. R., Millman, K. J., van der Walt, S. J., et al. 2020, Natur, 585, 357
Hartley, A. I., Nelson, E. J., Suess, K. A., et al. 2023, MNRAS, 522, 3138
Hashimoto, T., Álvarez-Márquez, J., Fudamoto, Y., et al. 2023, ApJL, 955, L2
Helton, J. M., Sun, F., Woodrum, C., et al. 2024, ApJ, 962, 124
Hill, R., Chapman, S., Scott, D., et al. 2020, MNRAS, 495, 3124
Hopkins, P. F., Hernquist, L., Cox, T. J., & Kereš, D. 2008, ApJS, 175, 356
Horne, K. 1986, PASP, 98, 609
Hu, W., Wang, J., Infante, L., et al. 2021, NatAs, 5, 485
Hunter, J. D. 2007, CSE, 9, 90
Ito, K., Tanaka, M., Miyaji, T., et al. 2022, ApJ, 929, 53
Ito, K., Tanaka, M., Valentino, F., et al. 2023, ApJL, 945, L9
Jin, S., Daddi, E., Liu, D., et al. 2018, ApJ, 864, 56
Jin, S., Sillassen, N. B., Magdis, G. E., et al. 2023, A&A, 670, L11
Johnson, B. D., Leja, J., Conroy, C., & Speagle, J. S. 2021, ApJS, 254, 22
Kalita, B. S., Daddi, E., D'Eugenio, C., et al. 2021, ApJL, 917, L17
Kawinwanichakij, L., Papovich, C., Quadri, R. F., et al. 2017, ApJ, 847, 134
Kewley, L. J., Geller, M. J., & Jansen, R. A. 2004, AJ, 127, 2002
Kriek, M., Price, S. H., Conroy, C., et al. 2019, ApJL, 880, L31
Kriek, M., van Dokkum, P. G., Labbé, I., et al. 2009, ApJ, 700, 221
Kubo, M., Umehata, H., Matsuda, Y., et al. 2021, ApJ, 919, 6
Kubo, M., Umehata, H., Matsuda, Y., et al. 2022, ApJ, 935, 89
Le Fèvre, O., Béthermin, M., Faisst, A., et al. 2020, A&A, 643, A1
Leja, J., Carnall, A. C., Johnson, B. D., Conroy, C., & Speagle, J. S. 2019, ApJ, 876, 3
Leja, J., Johnson, B. D., Conroy, C., van Dokkum, P. G., & Byler, N. 2017, ApJ, 837, 170
Lemaux, B. C., Le Fèvre, O., Cucciati, O., et al. 2018, A&A, 615, A77
Long, A. S., Antwi-Danso, J., Lambrides, E. L., et al. 2023, arXiv:2305.04662
Lustig, P., Strazzullo, V., D'Eugenio, C., et al. 2021, MNRAS, 501, 2659
Madau, P. 1995, ApJ, 441, 18
Man, A., & Belli, S. 2018, NatAs, 2, 695

Marsan, Z. C., Marchesini, D., Brammer, G. B., et al. 2015, ApJ, 801, 133
Maseda, M. V., van der Wel, A., Franx, M., et al. 2021, ApJ, 923, 18
McConachie, I., Wilson, G., Forrest, B., et al. 2022, ApJ, 926, 37
McCracken, H. J., Milvang-Jensen, B., Dunlop, J., et al. 2012, A&A, 544, A156
McLean, I. S., Steidel, C. C., Epps, H. W., et al. 2010, Proc. SPIE, 7735, 568
McLean, I. S., Steidel, C. C., Epps, H. W., et al. 2012, Proc. SPIE, 8446, 149
Merlin, E., Fortuni, F., Torelli, M., et al. 2019, MNRAS, 490, 3309
Miettinen, O., Delvecchio, I., Smolčić, V., et al. 2017, A&A, 606, A17
Miller, T. B., Chapman, S. C., Aravena, M., et al. 2018, Natur, 556, 469
Morishita, T., Abramson, L. E., Treu, T., et al. 2019, ApJ, 877, 141
Morishita, T., Roberts-Borsani, G., Treu, T., et al. 2023, ApJL, 947, L24
Nanayakkara, T., Glazebrook, K., Jacobs, C., et al. 2024, NatSR, 14, 3724
Nelan, J. E., Smith, R. J., Hudson, M. J., et al. 2005, ApJ, 632, 137
Nelson, D., Springel, V., Pillepich, A., et al. 2019, ComAC, 6, 2
Newman, A. B., Ellis, R. S., Bundy, K., & Treu, T. 2012, ApJ, 746, 162
Oke, J. B., & Gunn, J. E. 1983, ApJ, 266, 713
Onodera, M., Carollo, C. M., Renzini, A., et al. 2015, ApJ, 808, 161
Onodera, M., Renzini, A., Carollo, M., et al. 2012, ApJ, 755, 26
Oteo, I., Ivison, R. J., Dunne, L., et al. 2018, ApJ, 856, 72
Overzier, R. A. 2016, A&ARv, 24, 14
Peng, Y. j., Lilly, S. J., Kovač, K., et al. 2010, ApJ, 721, 193
Pillepich, A., Nelson, D., Hernquist, L., et al. 2018, MNRAS, 475, 648
Renzini, A. 2006, ARA&A, 44, 141
Sargent, M. T., Daddi, E., Bournaud, F., et al. 2015, ApJL, 806, L20
Schreiber, C., Glazebrook, K., Nanayakkara, T., et al. 2018, A&A, 618, A85
Schreiber, C., Pannella, M., Elbaz, D., et al. 2015, A&A, 575, A74
Scoville, N., Aussel, H., Brusa, M., et al. 2007, ApJS, 172, 1
Shimakawa, R., Koyama, Y., Röttgering, H. J. A., et al. 2018, MNRAS, 481, 5630
Shuntov, M., McCracken, H. J., Gavazzi, R., et al. 2022, A&A, 664, A61
Skrutskie, M. F., Cutri, R. M., Stiening, R., et al. 2006, AJ, 131, 1163
Smolčić, V., Delvecchio, I., Zamorani, G., et al. 2017, A&A, 602, A2
Stockmann, M., Toft, S., Gallazzi, A., et al. 2020, ApJ, 888, 4
Sun, F., Helton, J. M., Egami, E., et al. 2024, ApJ, 961, 69
Suzuki, T. L., Glazebrook, K., Schreiber, C., et al. 2022, ApJ, 936, 61
Tacchella, S., Conroy, C., Faber, S. M., et al. 2022, ApJ, 926, 134
Tanaka, M. 2015, ApJ, 801, 20
Tanaka, M., Onodera, M., Shimakawa, R., et al. 2023, arXiv:2311.11569
Tanaka, M., Valentino, F., Toft, S., et al. 2019, ApJL, 885, L34
Thomas, D., Maraston, C., Bender, R., & Mendes de Oliveira, C. 2005, ApJ, 621, 673
Thomas, D., Maraston, C., Schawinski, K., Sarzi, M., & Silk, J. 2010, MNRAS, 404, 1775
Toft, S., Gallazzi, A., Zirm, A., et al. 2012, ApJ, 754, 3
Toft, S., Smolčić, V., Magnelli, B., et al. 2014, ApJ, 782, 68
Toshikawa, J., Kashikawa, N., Overzier, R., et al. 2014, ApJ, 792, 15
Valentino, F., Brammer, G., Gould, K. M. L., et al. 2023, ApJ, 947, 20
Valentino, F., Tanaka, M., Davidzon, I., et al. 2020, ApJ, 889, 93
van der Wel, A., Franx, M., van Dokkum, P. G., et al. 2014, ApJ, 788, 28
van Dokkum, P. G., Franx, M., Kriek, M., et al. 2008, ApJL, 677, L5
Weaver, J. R., Davidzon, I., Toft, S., et al. 2023, A&A, 677, A184
Weaver, J. R., Kauffmann, O. B., Ilbert, O., et al. 2022, ApJS, 258, 11
Whitaker, K. E., Kriek, M., van Dokkum, P. G., et al. 2012, ApJ, 745, 179
Whitaker, K. E., Williams, C. C., Mowla, L., et al. 2021, Natur, 597, 485
Williams, C. C., Spilker, J. S., Whitaker, K. E., et al. 2021, ApJ, 908, 54
Williams, R. J., Quadri, R. F., Franx, M., van Dokkum, P., & Labbé, I. 2009, ApJ, 691, 1879
Yan, R., Newman, J. A., Faber, S. M., et al. 2006, ApJ, 648, 281
Young, J. S., & Scoville, N. Z. 1991, ARA&A, 29, 581
Zavala, J. A., Casey, C. M., Spilker, J., et al. 2022, ApJ, 933, 242